



Full Length Article

Simulations of rotating detonation combustion with *in-situ* evaporating bi-disperse *n*-heptane sprays

Shan Jin^{a,b}, Huangwei Zhang^{b,*}, Ningbo Zhao^a, Hongtao Zheng^a^a College of Power and Energy Engineering, Harbin Engineering University, Harbin 150001, China^b Department of Mechanical Engineering, National University of Singapore, 9 Engineering Drive 1, Singapore 117576, Republic of Singapore

ARTICLE INFO

Keywords:

Rotating detonation combustion
N-heptane spray
 Reactant mixing
 Equivalence ratio
 Velocity deficit
 Propulsion performance

ABSTRACT

Eulerian-Lagrangian simulations are conducted for two-dimensional Rotating Detonative Combustion fueled by bi-disperse *n*-heptane sprays without any fuel pre-vaporization. Parametric studies are performed to study the influences of droplet diameter and droplet distribution on the rotating detonation wave. The extinction process of the detonation wave is also analyzed. It is found that small *n*-heptane droplets (e.g., 2 μm) are completely vaporized in the fuel refilling area. Increasing the droplet diameter causes the droplet to fail to evaporate completely within the fuel refilling area and exist after the detonation wave. A reflected shock can be observed after the detonation wave. When the droplet diameter is larger than 10 μm, the higher pressure after the detonation wave leads to the reactants cannot be sprayed into the combustor, eventually leading to extinction of the detonation wave. In bi-disperse *n*-heptane sprays, presence of droplets with small diameter stabilizes the detonation wave. The average equivalence ratio (up to 0.66 only) in the fuel refilling area is lower than total equivalence ratio (1.0 in this work), and the average equivalence ratio decreases with increased droplet diameter in the bi-disperse *n*-heptane sprays. The increase in droplet diameter decreases the detonated fuel fraction and detonation wave speed. The detonation speeds in bi-disperse *n*-heptane sprays are 3–9% lower than the respective gaseous cases. Moreover, the results also show that propulsion performance of rotating detonation combustor, such as thrust and specific impulse, decreases with the droplet diameter.

1. Introduction

Rotating Detonation Engine (RDE) is deemed one of the most promising pressure-gain combustion technologies due to the high thermodynamic cycle efficiency [1,2]. In previous studies, gaseous fuels are mainly tested, including hydrogen and simple hydrocarbons [1–5]. However, liquid fuels typically have a higher energy density and are more convenient to be stored and transported. Utilization of liquid fuels is of utmost importance to commercialize rotating detonation technology to engineering practice.

The first liquid fuel RDE test was carried out in 1960s [6], and in recent years a lot of research progress has been available for liquid fuel RDEs. For instance, Bykovskii et al. [5,7,8] used liquid kerosene sprays and oxygen-enriched air in experimental research on two-phase rotating detonation. The diameter of outer combustor wall in their test was 306 mm. They found that addition of hydrogen to the mixture can reduce the critical diameter of the RDE combustor. After that, they increased the diameter to 503 mm [7,8], and found that the Rotating Detonation Wave

(RDW) cannot continuously propagate without hydrogen or syngas added.

In addition, Kindracki [9] investigated kerosene atomization characteristics under different carrier gas (nitrogen) velocities and fuel injection patterns in a RDE combustor. They measured the droplet diameters and found that when the sprayed droplet diameters are 20–40 μm, the droplets can quickly evaporate in the combustor. Subsequently, they used kerosene with hydrogen addition to conduct a two-phase rotating detonation experiment [10]. They successfully obtained a rotating detonation wave that propagates stably, with a velocity deficit of the detonation wave propagation being 20%–25%. More recently, Wolański and his co-workers [11] partially mixed the preheated liquid Jet-A and hot air, leading to a composition higher than the rich flammability limit. With that, they achieved a rotating detonation without hydrogen addition. They also found that heat losses, momentum losses, and pre-combustion of the fuel are the main reasons for the speed deficit (up to 35%).

To obtain more detailed structures of rotating detonations in liquid fuel sprays, RDE modelers also carried out a series of numerical studies.

* Corresponding author.

E-mail address: huangwei.zhang@nus.edu.sg (H. Zhang).<https://doi.org/10.1016/j.fuel.2021.123087>

Received 27 September 2021; Received in revised form 26 December 2021; Accepted 28 December 2021

0016-2361/© 2021 Elsevier Ltd. All rights reserved.

Nomenclature			
C_p	Heat capacity at constant pressure [J/kg/K]	Y_m	Mass fraction of m -th species
\mathbf{D}	Deformation gradient tensor	p	Pressure [Pa]
D_f	Vapour mass diffusivity in the gas phase [m ² /s]	X_S	Fuel vapor mole fraction
D_m	Mass diffusivity [m ² /s]	\mathbf{F}_d	Drag force on the droplet [N]
d_s^0	Initial droplet diameter of small droplet [μm]	\mathbf{F}_p	Pressure gradient force [N]
d_l^0	Initial droplet diameter of large droplet [μm]	F_u	Thrust from kinetic energy [N]
E	Total non-chemical energy [J/kg]	F_p	Thrust from pressure gain [N]
e	Specific sensible internal energy [J/kg]	A_0	Surface of outlet [m ²]
\mathbf{F}_d	Drag force on the droplet [N]	v_g	velocity of gaseous detonation [m/s]
$\Delta h_{f,m}^0$	Formation enthalpy of m -th species [J/mol]	v_d	velocity of two-phase detonations [m/s]
$h(T_d)$	Heat of vaporization at the droplet temperature [J/kg]	\dot{Q}_{lat}	Latent heat transfer rate [J/s]
\mathbf{I}	Unit tensor		
\mathbf{j}	Diffusive heat flux [W/m ²]	<i>Greek letters</i>	
k	Thermal conductivity coefficient [W/m/K]	α	Thermal diffusivity coefficient [m ² /s]
k_c	Mass transfer coefficient [m/s]	μ	Dynamic viscosity [kg/m/s]
Le_m	Lewis number of m -th species	ρ	Gas density [kg/m ³]
M	Total species number	ρ_d	Droplet material density [kg/m ³]
m_d	Mass of a single droplet [kg]	$\dot{\omega}_m$	Production or consumption rate of m -th species [kg/m ³ /s]
\dot{m}_d	Evaporation rate [kg/s]	$\dot{\omega}_T$	Heat release from chemical reactions [J/m ³ /s]
\dot{m}_f	Vapor mass flux [kg/m ² /s]	ϕ	Equivalence ratio
$C_{p,d}$	droplet heat capacity [J/kg/K]	ψ	detonated fuel fraction
Nu	Nusselt number		
n_p	Droplet number per parcel	<i>Superscript</i>	
T_S	Droplet surface temperature [K]	0	Initial value
V_d	Volume of a single fuel droplet [m ³]		
B_T	Spalding heat transfer number	<i>Subscripts</i>	
Pr	Prandtl number	c	CFD cell
Re_d	Droplet Reynolds number	d	Droplet
\dot{Q}_c	Convective heat transfer rate [J/s]	<i>energy</i>	Energy
R	Specific gas constant [J/kg/K]	f	Droplet surface
R_u	Universal gas constant [J/mol/K]	i	i -th condensed species vapor
Sc	Schmidt number	m	Mass, m -th species
Sh	Sherwood number	<i>mass</i>	Mass
s_m	Species mass flux [kg/m ² /s]	<i>mom</i>	Momentum
S_{mass}	Mass transfer rate [kg/m ³ /s]	p	Pressure gain
S_{mom}	Momentum transfer rate [N/m ³]	s	Small droplet
S_{energy}	Energy transfer rate [J/m ³ /s]	<i>species</i>	Species
$S_{species,m}$	Species transfer rate [kg/m ³ /s]	l	Large droplet
T	Gas temperature [K]	<i>eff</i>	Effective value
\mathbf{T}	Viscous stress tensor [kg/m/s ²]	u	kinetic energy
T_d	Droplet temperature [K]		
t	Time [s]	<i>Acronym</i>	
\mathbf{u}	Velocity vector [m/s]	RDE	Rotating detonation engine
\mathbf{u}_d	Droplet velocity vector [m/s]	RDW	Rotating detonation wave
V_c	CFD cell volume [m ³]	HRR	Heat release rate [J/m ³ /s]
W_d	Molar weight of the vapor [kg/mol]	ER	Evaporation rate [kg/m ³ /s]
W_m	Molar weight of m -th species [kg/mol]	FI	Flame index
		I_{sp}	Specific impulse [s]
		CFD	Computational fluid dynamics

For instance, Sun and Ma [12] investigated the effects of air total temperature and fuel inlet spacing on the two-phase RDW in liquid octane and air. They found that increasing the fuel inlet spacing decreases the wave speed. Moreover, Hayashi et al. [13] investigated the effects of JP-10 droplet diameter and pre-evaporation on two-phase rotating detonation waves. They found that there are liquid droplets along the contact surface between the fresh and burned gas. Ren and Zheng [14] studied the limit of kerosene/air two-phase detonation stability as a function of total pressure and total temperature, mimicking the operating conditions of ramjet detonation engine. They found that stable rotating detonation can be achieved in a limited range of total pressure and increased total temperature is conducive to RDW stability.

Moreover, Meng et al. [15] used n -heptane/air as the reactants to systematically study the influences of initial droplet diameter (5–50 μm) and the n -heptane pre-evaporation degree on detonation characteristics (e.g., detonation velocity, detonated fuel fraction, droplet evaporation height). Meng et al. [16] also investigated the rotating detonation combustion with partially pre-vaporised n -heptane spray without hydrogen addition. They analyzed the detailed RDE flow field and droplet distribution inside the fuel refilling zone and found that a layer with high vapor concentration exists between the droplet-laden area and deflagration surface. Besides, Zhao and Zhang [17] investigated the influences of droplet diameter and equivalence ratio on rotating detonations. The propagation speed increases as the total equivalence ratio

increases for the same droplet diameter. Furthermore, they observed that when the droplet diameter is less than 5 μm , the thrust force from pressure gain and kinetic energy decreases significantly with the droplet diameter. However, for initial droplet diameter $d_0 > 5 \mu\text{m}$, the thrust force from the kinetic energy first increases and then decreases with the droplet diameter, while the thrust force from pressure gain is shown to have limited change.

In this work, the effects of initial droplet diameter on wave speed, detonated fuel fraction and specific impulse in two-phase rotating detonation combustor without pre-vaporization (only *in-situ* gasification) will be further studied with Eulerian–Lagrangian method. In previous studies on two-phase detonation, mono-sized or polydispersed droplets have been considered, such as in Refs. [13,14,18–21]. It is well known that the droplets of various sizes can behave differently in terms of evaporation, heating and velocity relaxation with the gas phase. When we consider the mono-sized droplets, it is possible to clearly understand how the droplets of a particular size evolve in a detonated flow field. However, this is idealized, because polydisperse droplets are ubiquitous in practical spray combustion because atomizers are used [9–11]. Nonetheless, a real droplet size distribution (i.e., diameter range and distribution shape) is still full of uncertainties (difficult to be characterized) and it is challenging to be accurately modelled in CFD. If we use some presumed distributions for the droplets, this will make our research results lack of generality. Therefore, we will consider bi-disperse droplets in this study. Two-dimensional flatten domain is used to model the practical rotating detonation combustor, and liquid *n*-heptane and air are selected as the reactants. The rest of the manuscript is structured as below. In Section 2 the computational method and the physical model are introduced. Results are presented and discussed in Section 3, whereas conclusions are made in Section 4.

2. Mathematical and physical models

2.1. Governing equation

The Eulerian–Lagrangian method is used to investigate the two-phase rotating detonation combustion in this work. The gas phase is described with the Eulerian method, whilst the sprayed liquid fuel droplets are tracked by the Lagrangian method. For the gas phase, the governing equations for unsteady compressible multi-species reacting flows read

$$\frac{\partial \rho}{\partial t} + \nabla \cdot [\rho \mathbf{u}] = S_m \quad (1)$$

$$\frac{\partial (\rho \mathbf{u})}{\partial t} + \nabla \cdot [\mathbf{u}(\rho \mathbf{u})] + \nabla p + \nabla \cdot \mathbf{T} = S_F \quad (2)$$

$$\frac{\partial (\rho E)}{\partial t} + \nabla \cdot [\mathbf{u}(\rho E)] + \nabla \cdot [\rho \mathbf{u} p] + \nabla \cdot [\mathbf{T} \cdot \mathbf{u}] + \nabla \cdot \mathbf{j} = \underline{a}_T + S_e \quad (3)$$

$$\frac{\partial (\rho Y_m)}{\partial t} + \nabla \cdot [\mathbf{u}(\rho Y_m)] + \nabla \cdot \mathbf{s}_m = \underline{a}_m + S_{Y_m}, \quad (m = 1, \dots, M-1) \quad (4)$$

$$p = \rho RT \quad (5)$$

here t is time and $\nabla \cdot (\cdot)$ is the divergence operator. ρ is the gas density, \mathbf{u} is the gas velocity vector, T is the gas temperature, and p is the pressure. Y_m is the mass fraction of m -th species, and M is the total species number. E is the total non-chemical energy, i.e., $E \equiv e_s + |\mathbf{u}|^2/2$. $e_s = h_s - p/\rho$ is the sensible internal energy and h_s is sensible enthalpy. R in Eq. (5) is the specific gas constant and is calculated from $R = R_u \sum_{m=1}^M Y_m MW_m^{-1}$. MW_m is the molar weight of m -th species and $R_u = 8.314 \text{ J}/(\text{mol} \cdot \text{K})$ is the universal gas constant. The viscous stress tensor \mathbf{T} in Eq. (2) modelled by $\mathbf{T} = -2\mu \text{dev}(\mathbf{D})$. Here μ is the dynamic viscosity and is dependent on gas temperature following the Sutherland's law. Moreover,

$\mathbf{D} \equiv [\nabla \mathbf{u} + (\nabla \mathbf{u})^T]/2$ is the deformation gradient tensor and its deviatoric component, $\text{dev}(\mathbf{D})$, is defined as $\text{dev}(\mathbf{D}) \equiv \mathbf{D} - \text{tr}(\mathbf{D})\mathbf{I}/3$ with \mathbf{I} being the unit tensor. \mathbf{j} in Eq. (3) is the diffusive heat flux and can be modelled by Fourier's law, i.e. $\mathbf{j} = -k\nabla T$. Thermal conductivity k is calculated using the Eucken approximation [22], i.e. $k = \mu C_v(1.32 + 1.37 \cdot R/C_v)$, where C_v is the heat capacity at constant volume and derived from $C_v = C_p - R$. Here $C_p = \sum_{m=1}^M Y_m C_{p,m}$ is the heat capacity at constant pressure, and $C_{p,m}$ is the heat capacity of m -th species, which is estimated from JANAF polynomials [23]. Particle-source-in-cell (PSI-CELL) approach is used [24] and the source terms in Eqs. (1)–(4), i.e., S_m , S_F , S_e and S_{Y_m} , account for the exchanges of mass (fuel species), momentum, and energy, respectively.

In Eq. (4), $\mathbf{s}_m = -D_m \nabla(\rho Y_m)$ is the species mass flux. With unity Lewis number assumption, the mass diffusivity D_m is calculated through $D_m = k/\rho C_p$. Moreover, $\dot{\omega}_m$ is the production or consumption rate of m -th species by all N reactions, and can be calculated from the reaction rate of each reaction $\omega_{m,j}^0$, i.e.

$$\dot{\omega}_m = MW_m \sum_{j=1}^N \omega_{m,j}^0 \quad (6)$$

Also, the term $\dot{\omega}_T$ in Eq. (3) accounts for the heat release from chemical reactions and is estimated as $\dot{\omega}_T = -\sum_{m=1}^M \dot{\omega}_m \Delta h_{f,m}^0$. Here $\Delta h_{f,m}^0$ is the formation enthalpy of m -th species.

The Lagrangian method is used to track the liquid fuel droplets. The equations of mass, momentum, and energy for single droplets are

$$\frac{dm_d}{dt} = -\dot{m}_d, \quad (7)$$

$$\frac{d\mathbf{u}_d}{dt} = \frac{\mathbf{F}_d + \mathbf{F}_p}{m_d}, \quad (8)$$

$$c_{p,d} \frac{dT_d}{dt} = \frac{\dot{Q}_c + \dot{Q}_{lat}}{m_d}, \quad (9)$$

where $m_d = \pi \rho_d d^3/6$ is the mass of a single droplet, where ρ_d and d are the droplet material density and diameter, respectively. \mathbf{u}_d is the droplet velocity vector, $c_{p,d}$ is the droplet heat capacity, and T_d is the droplet temperature. Uniform temperature inside the droplet is assumed, since the droplet Biot number is small in our simulations.

Phase change of the liquid fuel droplets, i.e., evaporation, is considered in our studies. The phase transition can be described with the help of an equilibrium, or non-equilibrium model or a generalized model [25–27]. In this study, the evaporation rate of the droplet \dot{m}_d is calculated with Abramzon and Sirignano model [28]. Its accuracy in prediction of droplet evaporation in elevated ambient pressures and temperatures has been validated in our recent work [17]. The droplet evaporation rate reads

$$\dot{m}_d = \pi d \rho_f D_f Sh \ln(1 + B_M) \quad (10)$$

where $\rho_f = p_S MW_m / RT_S$ and $D_f = 3.6059 \times 10^{-3} \cdot (1.8T_S)^{1.75} \cdot (\alpha/p_S \beta)$ are the density and mass diffusivity at the film over the droplet, respectively [17]. α and β are the constants related to specific species [29]. $p_S = p \cdot \exp(c_1 + c_2/T_S + c_3 \ln T_S + c_4 T_S^5)$ is the surface vapor pressure, with $T_S = (T + 2T_d)/3$ being the droplet surface temperature. In Eq. (10), B_M is the Spalding mass transfer number and defined as $B_M \equiv (Y_{F_S} - Y_{F_\infty})/(1 - Y_{F_S})$. $Y_{F_S} = MW_d X_S / [MW_d X_S + MW_{ed}(1 - X_S)]$ and Y_{F_∞} are the vapor mass fractions at the droplet surface and in the gas phase, respectively. MW_d is the molecular weight of the vapor, MW_{ed} is the averaged molecular weight of the mixture excluding the fuel vapor, and $X_S = X_m p_{sat}/p$ is the mole fraction of the vapor at the droplet surface. Here p_{sat} is the saturated pressure and X_m is the molar fraction of the condensed species in the gas phase.

In Eq. (8), \mathbf{F}_d is the Stokes drag, which is modelled as

$\mathbf{F}_d = \left(18\mu/\rho_d d^2\right) \cdot (C_d Re_d/24) \cdot m_d(\mathbf{u} - \mathbf{u}_d)$ [30]. Here C_d is the drag coefficient and estimated using the Schiller and Naumann model [31]. $Re_d \equiv \rho d|\mathbf{u}_d - \mathbf{u}|/\mu$ is the droplet Reynolds number. Also, \mathbf{F}_p is the pressure gradient force and is calculated from $\mathbf{F}_p = -V_d \nabla p$. Here V_d is the volume of a single fuel droplet.

In Eq. (9), $\dot{Q}_c = h_c A_d (T - T_d)$ denotes the convective heat transfer between the gas and liquid phases. Here A_d is surface area of a single droplet. h_c is the convective heat transfer coefficient, and estimated using the correlation of Ranz and Marshall [32] through the modified Nusselt number, i.e. $Nu = 2 + \left[(1 + Re_d Pr)^{1/3} \max(1, Re_d)^{0.077} - 1 \right] / F(B_T)$ [28]. Pr is the gas Prandtl number, and B_T is the Spalding heat transfer number. Furthermore, \dot{Q}_{lat} in Eq. (9) denotes the heat transfer caused by the latent heat of evaporation.

Two-way coupling between the gas and liquid phases are considered based on PSI-CELL method, in terms of mass, momentum, energy and species exchanges. Specifically, we consider the transfer of the fuel species between liquid droplets and the gas due to liquid evaporation. We also include the convective heat transfer between the gas and liquid phases and the heat transfer caused by the enthalpy carried by the fuel vapour. Besides, the drag force and momentum transfer due to droplet evaporation are taken into consideration, and the gravitational force is neglected since we only study small droplets. Therefore, the source terms for the gas phase equations read (V_c is cell volume and N_d is the droplet number in a CFD cell)

$$S_m = \frac{1}{V_c} \sum_1^{N_d} \dot{m}_d, \quad (11)$$

$$\mathbf{S}_F = -\frac{1}{V_c} \sum_1^{N_d} \left(-\dot{m}_d \mathbf{u}_d + \mathbf{F}_d \right), \quad (12)$$

$$S_e = -\frac{1}{V_c} \sum_1^{N_d} \left[-\dot{m}_d h(T_d) + \dot{Q}_c \right], \quad (13)$$

$$S_{Y_m} = \begin{cases} S_m \text{ for the liquid fuel species,} \\ 0 \text{ for other species,} \end{cases} \quad (14)$$

In Eq. (13), $h(T_d)$ is the fuel vapor enthalpy at the droplet temperature. Note that the energy exchange caused by the hydrodynamic force is not included since it is of secondary importance for dilute spray detonations [33]. This has also been confirmed from our *a posteriori* comparisons of the hydrodynamic force work and convective heat transfer from our simulations, which shows that the former is much (2–3 orders of magnitude) smaller than the latter in dilute and fine sprays.

2.2. Physical model

Fig. 1 shows the schematic of rotating detonation in a two-dimensional (2D) unrolled model RDE chamber. Although three-dimensional (3D) geometry effects do play an essential role in rotating detonations [4,34–37], however, the objective of this paper is to investigate the effects of dispersed phase properties (such as droplet size and loading) on rotating detonations, and it is sufficient if we can well predict the key flow field characteristics in the modelled RDE combustor. Previous studies using 2D domain have confirmed that 2D simulations can accurately reproduce the flow and combustion features in RDEs, e.g., in Refs. [38,39]. In light of these considerations, in this paper, a 2D computational domain will be adopted. The lengths (x -direction) and width (y -direction) of the domain are 153 mm and 50 mm, respectively. This extent ensures that the rotating detonation wave and accompanied flow features can be correctly captured.

The boundary conditions of the model RDE chamber are also marked in Fig. 1. Specifically, the outlet is assumed to be non-reflective, which is reasonable since the local flows are supersonic. Periodic boundaries at the left and right sides are enforced, such that the RDW can continuously propagate across the flattened domain.

Through the continuous injectors at the bottom of the domain in Fig. 1, the spherical droplets of liquid n -heptane sprays are injected into the domain with carrier gas, heated air, with the same strategy used by Meng et al. [15,16]. The initial temperature of the n -heptane droplets is 323 K to promote rapid evaporation of the droplet. The initial material density of the n -heptane droplets is 680 kg/m³. The initial temperature and pressure of the carrier gas air are 700 K and 30 atm, respectively. The liquid equivalence ratio can be varied by changing volume fractions of the liquid fuel droplets in the carrier gas. Moreover, a high-temperature and high-pressure spot (2,000 K and 20 atm) of 1 mm \times 12 mm is used in the lower left corner of the combustor, as shown in Fig. 1, to initiate the detonation wave.

It is well known that in practical RDEs [9–11], liquid fuel sprays are always polydispersed, and the size of the fuel droplets are therefore distributed. Different from our previous work [15–17], the effects of the initial droplet diameters of a polydisperse sprays on RDW propagation, in-chamber reactant mixing and propulsion performance are studied. However, to pinpoint the foregoing effects, bi-dispersed droplets with a specified mass ratio are considered in the current study, i.e., one class of fuel droplets with smaller diameter d_s^0 , whilst the other class with larger sizes d_l^0 . Their mass ratios are parameterized by liquid equivalence ratios, i.e., ϕ_s and ϕ_l , respectively. They are defined as the mass ratio of the liquid droplets (with d_s^0 and d_l^0) to the carrier gas air from the injector. In all the simulations, the total liquid fuel equivalence ratios, i.e., $\phi_t = \phi_s + \phi_l$, are fixed to be unity. As such, varying either of the equivalence ratio, ϕ_s or ϕ_l , would lead to change of the other. The initial diameter of the

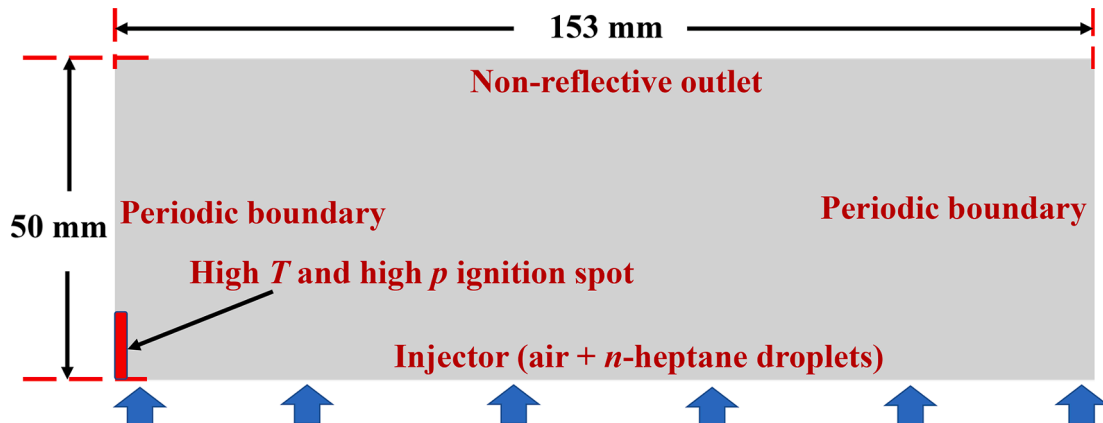


Fig. 1. Computational domain and boundary condition in two-dimensional RDE.

smaller droplet class d_s^0 is fixed to be $2\ \mu\text{m}$ in all our cases, whereas d_l^0 varies from 5 to $20\ \mu\text{m}$.

Moreover, in this study, pure *n*-heptane sprays with *in-situ* evaporation in the RDE model combustor will be considered, i.e., no pre-vaporization effects. Therefore, this is closer to the practical RDE implementations. In published literature, very limited work has been reported on modelling of pure spray RDE, except the recent one by Ren and Zheng [14], where pure kerosene is used as the propellant.

2.3. Numerical implementation

The governing equations for both gas and liquid phases are solved by a multiphase reacting flow code *RYrhoCentralFoam* [40], which is developed based on a density-based compressible flow solver *rhoCentralFoam* in OpenFOAM 6.0 [41]. Detailed validations and verifications have been made for *RYrhoCentralFoam* [42,43], including: (1) shock capturing, (2) molecular diffusion, (3) shock-chemistry interactions, (4) chemistry integration schemes, (5) detonation propagation speed and cellular structure, and (6) gas–liquid two-phase models (such as droplet evaporation, two-phase coupling). All the validations are demonstrated collectively through Ref. [44]. It has been successfully used for modelling detonative combustion with gaseous and liquid fuels [15,17,39,44].

The cell-centered finite volume method is used to discretize the gas phase equations, i.e., Eqs. (1)–(4). The second-order implicit backward scheme is used for time marching of the gas phase variables. The time step is about 10^{-9} s, which leads to a maximum Courant number of 0.1. Moreover, second-order Godunov-type upwind-central scheme is used to calculate the convection terms in the momentum equations. The total variation diminishing scheme is applied for the convection terms in the energy and species mass fraction equations.

Two-step chemical mechanism for *n*-heptane is used in this work, which includes six species (i.e., *n*-C₇H₁₆, CO, CO₂, H₂O, O₂, N₂) and two reactions. The chemical mechanisms are listed in Table 1 with their respective parameters for Arrhenius kinetics. This mechanism has been validated against a detailed mechanism [45] and the results show that it can correctly reproduce the detonation propagation speed, pressure, and temperature at both von Neumann and Chapman–Jouguet (C-J) points in the ZND (Zeldovich – von Neumann – Döring) structures corresponding to a wide range of operating conditions [16]. The two-step chemistry is deemed sufficient in this work since detailed gaseous chemistry is not focused on here; instead, we are more interested in detonation propagation speed, overall propulsion performance and droplet dynamics in liquid fueled RDE.

For the liquid phase, the Lagrangian equations, i.e., Eqs. (7)–(9), are solved with the first-order Euler method. With the PSI-CELL implementations, two-way coupling between the gas and liquid phases about species, mass, momentum, and energy exchanges is performed for each time step, through Eqs. (11)–(14). The droplet breakup model by Reitz [46] is used, which can accurately simulate the droplet breakup under engine relevant conditions and also successfully used for spray detonation modelling [17]. We use computational parcel method in our simulations, and one parcel contain many droplets having the same velocity, size, temperature, and thermodynamic parameters. The droplets in each parcel will be solved from the same set of Lagrangian equations, i.e., Eqs. (7)–(9). The actual initial number of the droplets in a

Table 1

Chemical mechanism for *n*-C₇H₁₆ combustion (units in cm-sec-mole-cal-Kelvin). *A* is the pre-exponential factor, *n* is the temperature exponent, *E_a* is the activation energy, *a* and *b* are the fuel and oxidizer reaction orders, respectively.

Reaction	<i>A</i>	<i>n</i>	<i>E_a</i>	<i>a</i>	<i>b</i>
I $2n\text{-C}_7\text{H}_{16} + 15\text{O}_2 \Rightarrow 14\text{CO} + 16\text{H}_2\text{O}$	6.3×10^{11}	0.0	30,000.0	0.25	1.5
II $2\text{CO} + \text{O}_2 \Leftrightarrow 2\text{CO}_2$	4.5×10^{10}	0.0	20,000.0	1.0	0.5

parcel are determined from the loading and diameter of the droplets.

The computational domain in Fig. 1 is discretized with uniform 496,000 Cartesian cells for the Eulerian flow field calculations and the cell spacing size is $125\ \mu\text{m}$. Mesh sensitivity analysis is also performed, which demonstrates that further refinement of the mesh would not change the predicted detonation speed and key features of the rotating detonative flow fields. Additionally, in the hybrid Eulerian – Lagrangian method with point-force approximation, the Lagrangian droplet diameter should be smaller than the Eulerian cell size [47]. This is because the gas phase quantities near the droplet surfaces (critical for estimating the two-phase coupling, e.g. evaporation) can be well approximated using the interpolated ones at the location of the sub-grid droplet [48]. In our simulations, the ratio of the Eulerian cell size and Lagrangian droplets, θ , range from 6.25 to 62.5, which is well above or close to the criterion, $\theta > 10$, as suggested by Sontheimer et al. [49] and Luo et al. [50]. As such, the current Eulerian mesh resolution is expected to be sufficient for capturing the flow field, droplet dynamic behaviors and gas – liquid bi-directional coupling in liquid fuel rotating detonations.

The accumulation error in numerical simulations depends on the accuracy of algorithm and grid, and the number of time integration steps. Some methods for error estimations in simulations of a combustor are provided in Refs. [51] and [52]. Based on their methods, the cumulative error in our simulations is about 0.3%, estimated with the numerical scheme accuracy (second-order), mesh size (0.125 mm), and time step (2×10^{-9} μs) used in this work. This confirms the accuracy of the numerical methods in *RYrhoCentralFoam* solver and simulation setup for the spray RDE modelling.

Note that the operating time of an RDE test can be, e.g., 0.1 s or 4 s [10,11]. Considering the computational cost, the simulated physical time of the rotating detonations in this paper are about 1,500 μs, which is indeed lower than the reported time in the actual experiments. Nonetheless, this roughly corresponds to 10 cycles of rotating detonations and the detonation wave has propagated steadily. Therefore, the long-term behaviors of the detonation wave can be well confirmed in our simulations.

3. Results and discussion

3.1. RDW propagation in fuel sprays

The features of rotating detonations in sprayed *n*-heptane fuels will be demonstrated in this section. Three cases are considered: (1) mono-sized sprays with initial droplet diameter $d^0 = 2\ \mu\text{m}$; (2) mono-sized sprays with $d^0 = 10\ \mu\text{m}$; and (3) bi-disperse sprays with 50% droplets of $d_s^0 = 2\ \mu\text{m}$ and 50% large droplets of $d_l^0 = 10\ \mu\text{m}$. Be reminded that the (total) liquid fuel equivalence ratios in these three cases are identical, i.e. $\phi_t = 1.0$. The key information about the gas phase and liquid phase is listed in Table 2.

Fig. 2 shows the contours of pressure and gas temperature corresponding to case 1. The results are extracted after the RDW runs over ten cycles. In this work, one cycle means that the RDW propagates from the left periodic boundary to the right one. The key features of rotating

Table 2

Information about the gas phase and liquid phase in cases 1–3. *T₀* and *p₀* are total temperature and total pressure of carrier air, ϕ_t is total liquid fuel equivalence ratio, T_d^0 is temperature of droplets, d^0 is mono-sized sprays with initial droplet diameter, d_s^0 and d_l^0 are initial droplet diameter of small droplets and large droplets in bi-disperse sprays.

Case	Gas phase		Liquid phase				
	<i>T₀</i> (K)	<i>p₀</i> (atm)	ϕ_t	<i>T_d⁰</i> (K)	<i>d⁰</i> (μm)	<i>d_s⁰</i> (μm)	<i>d_l⁰</i> (μm)
1	700	30	1	323	2	–	–
2					10	–	–
3					–	2	10

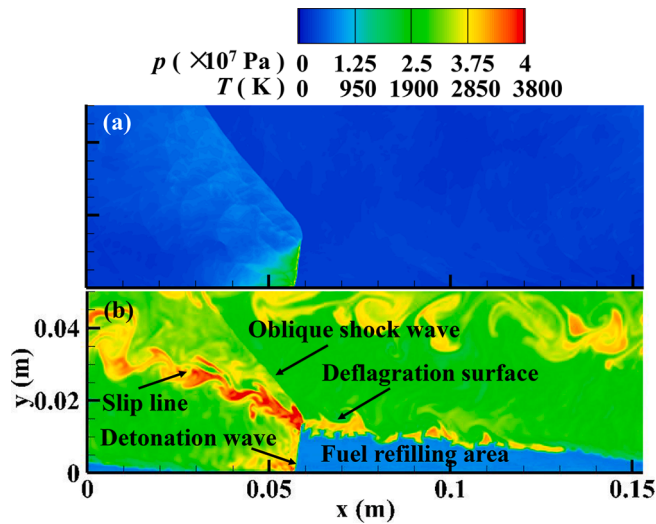


Fig. 2. Contours of (a) pressure and (b) gas temperature. $d^0 = 2 \mu\text{m}$ and $\phi_t = 1.0$.

detonation flow field, including detonation wave, oblique shock wave, slip line and deflagration surface, are well predicted, as marked in Fig. 2 (b). The triangular fuel refilling area is generally regular, and thereby liquid fuel evaporation and fuel vapor / oxidizer mixing can proceed therein. The average detonation propagation velocity of the detonation wave under the current condition is about 1760 m/s, which is lower than the purely gaseous RDW speed (1830 m/s) under the same pressure and total temperature conditions. The C-J speed in the corresponding gaseous conditions is 1835.7 m/s. As such, the velocity deficits are 3.8% and 4.1%, respectively.

Fig. 3 further shows the enlarged views about the distributions of Heat Release Rate (HRR), Evaporation Rate (ER), $n\text{-C}_7\text{H}_{16}$ vapor mass fraction, pressure gradient magnitude, Lagrangian droplet temperature and diameter near the detonation wave in Fig. 2. Note that in Fig. 3(b) the evaporation rate is the volumetric source term S_m in Eq. (11) and therefore it is a Eulerian quantity. One can see from Fig. 3(a) that high heat release rate can be found along the detonation wave, except near the triple point. There, the leading shock (solid line) and reaction front (with high HRR) are decoupled. This is because the fuel vapor ahead of it has been consumed by the deflagration surface.

After being injected into the combustor, the $n\text{-heptane}$ droplets are quickly heated close to the saturation temperature (see Fig. 3e, about 540 K) and then start to vaporize quickly and therefore considerable evaporation can be observed near the injector with fast reduction of the droplet size, demonstrated in Fig. 3(b) and 3(f). The height of the evaporating droplet layer is small, about 1.5 mm, beyond which no droplets exist. In the fuel filling area, the resultant $n\text{-heptane}$ vapor mass fraction is close to stoichiometry (about 6.02%, see Fig. 3c), indicating the complete evaporation of the liquid fuels. One can also see from Fig. 3 (c) that the fuel vapor mass fraction is relatively uniform ahead of the RDW, which implies the efficient mixing of the fuel vapor and oxidizer inside the refilling area. Moreover, it is shown from Fig. 3(c), 3(e) and 3 (f) that there are no $n\text{-heptane}$ droplets behind the detonation wave, and therefore all the fuels have been consumed by the rotating detonation wave or deflagration surface.

Fig. 4 shows the contours of pressure and gas temperature in case 2, in which the initial droplet diameter d^0 is increased to $10 \mu\text{m}$. In this case, the detonation wave is quenched after propagating after about 5 cycles. The transient extinction process will be discussed in detail in Section 3.2. Briefly, the fuel refilling area becomes less organized, compared to that in case 1. No pronounced temperature rise is observed along the interface between the fuel refilling area and burned product gas. This indicates that less deflagrative combustion occurs due to

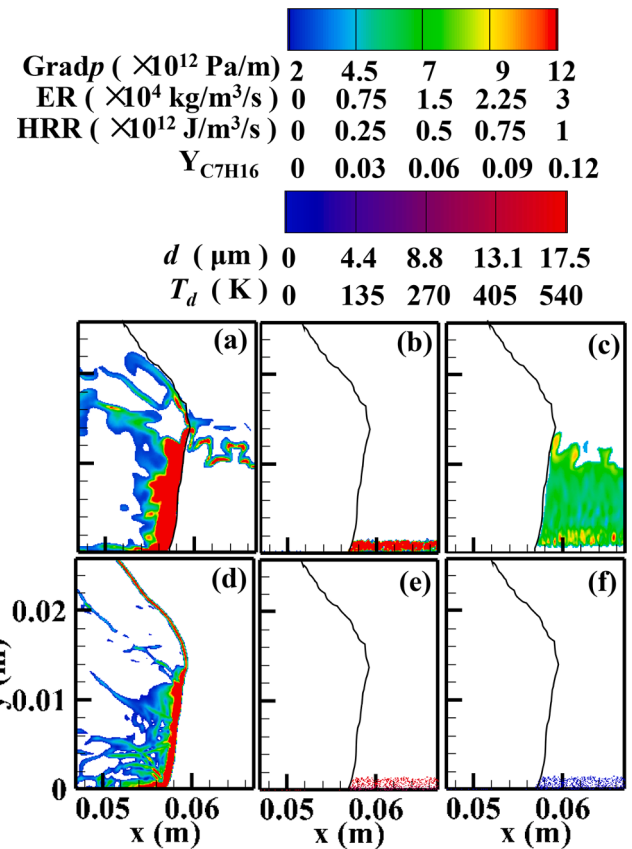


Fig. 3. Contours of (a) heat release rate, (b) evaporation rate, (c) $n\text{-heptane}$ vapor mass fraction, (d) pressure gradient magnitude, (e) droplet temperature and (f) diameter. $d^0 = 2 \mu\text{m}$ and $\phi_t = 1.0$. Solid line: detonation and oblique shock waves.

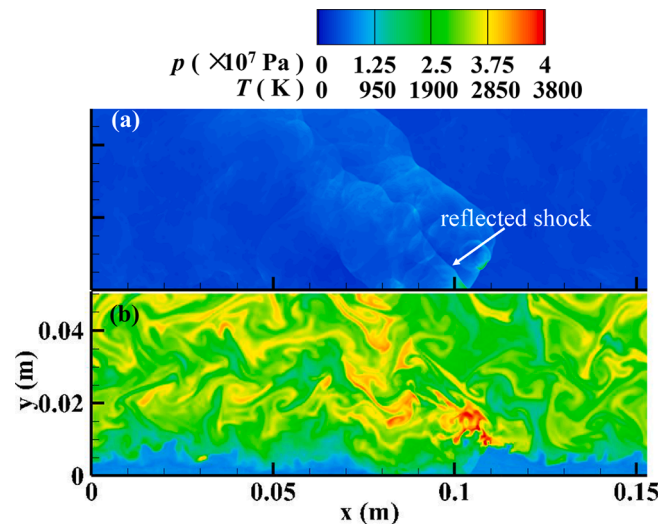


Fig. 4. Contours of (a) pressure and (b) gas temperature. $d^0 = 10 \mu\text{m}$ and $\phi_t = 1.0$.

insufficient fuel vapor. Moreover, the leading shock wave becomes oblique and is reflected at the inlet. Since the pressure immediately behind the RDW is higher than the total pressure, based on our gas injection method [15,16], it is assumed to be a solid wall. This reflected shock is almost parallel to the oblique shock connected with the leading shock.

Fig. 5 shows the distributions of HRR, ER, n -C₇H₁₆ vapor mass fraction, pressure gradient magnitude, Lagrangian droplet temperature and diameter around the detonation wave corresponding to the same instant in Fig. 4. The HRR contour in Fig. 5(a) shows that the detonative combustion only proceeds behind a small fraction of the leading shock, roughly corresponding to the downstream ($y > 0.006$ m) of the fuel refilling area. When $y < 0.006$ m, finite distance between the leading shock wave and reaction front can be seen, and therefore no detonations occur there. However, one can find that a Secondary Rotating Detonation Wave (SRDW) exists near the injector. This phenomenon is also reported by Ren and Zheng [14] in liquid kerosene RDE. The formation of SRDW can be attributed to: (1) existence of the reflected shock wave; (2) sufficient n -heptane vapor ahead of the reflected shock wave (behind the leading shock). The second reason can be more clearly shown in Fig. 5(b) and 5(c), through which high evaporation rate and fuel vapor concentration can be found between the reflected and leading shocks. How the secondary rotating detonation wave evolves during a detonation extinction process will be further interpreted in Section 3.2. In this case, the height of the evaporating droplet distribution zone is much higher than that in case 1, because larger droplets may have longer heating and evaporation timescales.

Plotted in Fig. 6 are the contours of pressure and gas temperature in the bidisperse sprays, i.e., case 3. Similar to the results of case 2 in Fig. 5, the leading shock wave is inclined, and a reflected shock wave is present. However, different from case 2, case 3 is characterized by continuously rotating detonation propagation across the model RDE chamber. Although the RDW are stable both in cases 1 and 3, nevertheless, the morphology of the RDW is different, which can be more clearly seen in Fig. 7.

Fig. 7 shows zoomed contours of the HRR, ER, n -C₇H₁₆ vapor mass

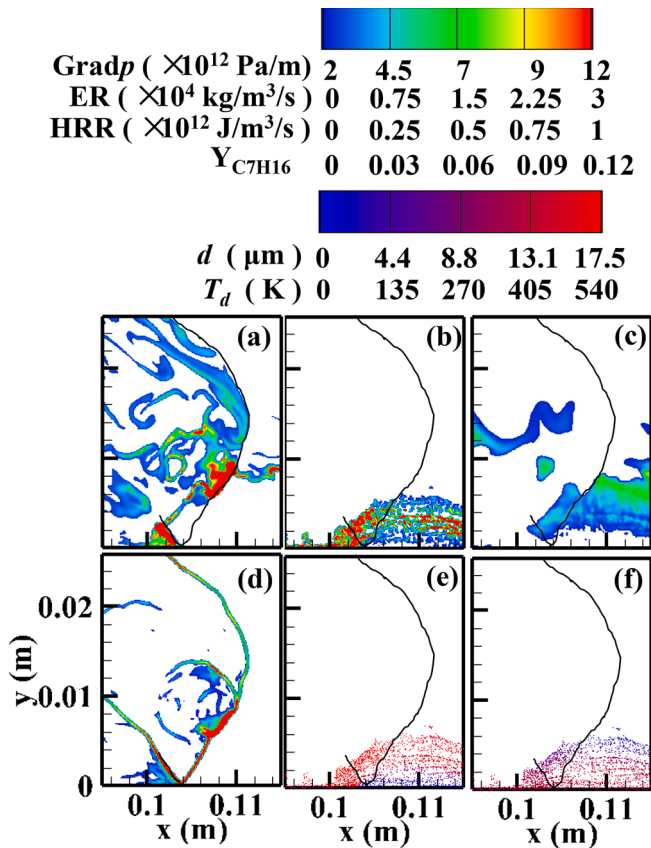


Fig. 5. Contours of (a) heat release rate, (b) evaporation rate, (c) n -heptane vapor mass fraction, (d) pressure gradient magnitude, (e) droplet temperature and (f) diameter. $d_s^0 = 10 \mu\text{m}$ and $\phi_t = 1.0$. Solid line: detonation and oblique shock waves.

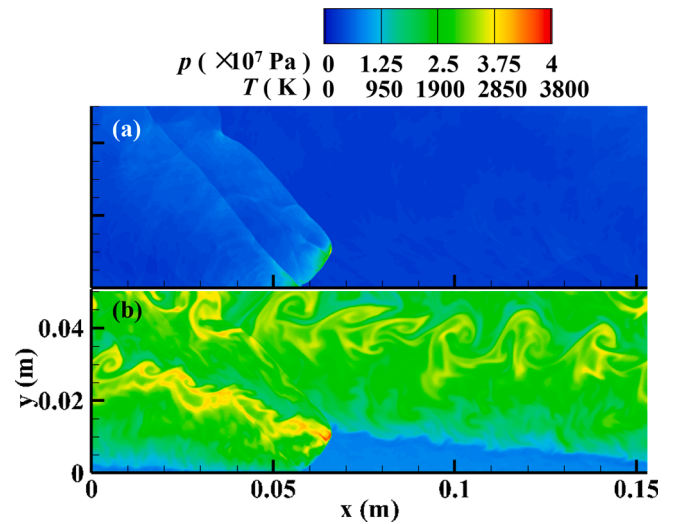


Fig. 6. Contours of (a) pressure and (b) gas temperature. $d_s^0 = 2 \mu\text{m}$ (50%), $d_l^0 = 10 \mu\text{m}$ (50%), and $\phi_t = 1.0$.

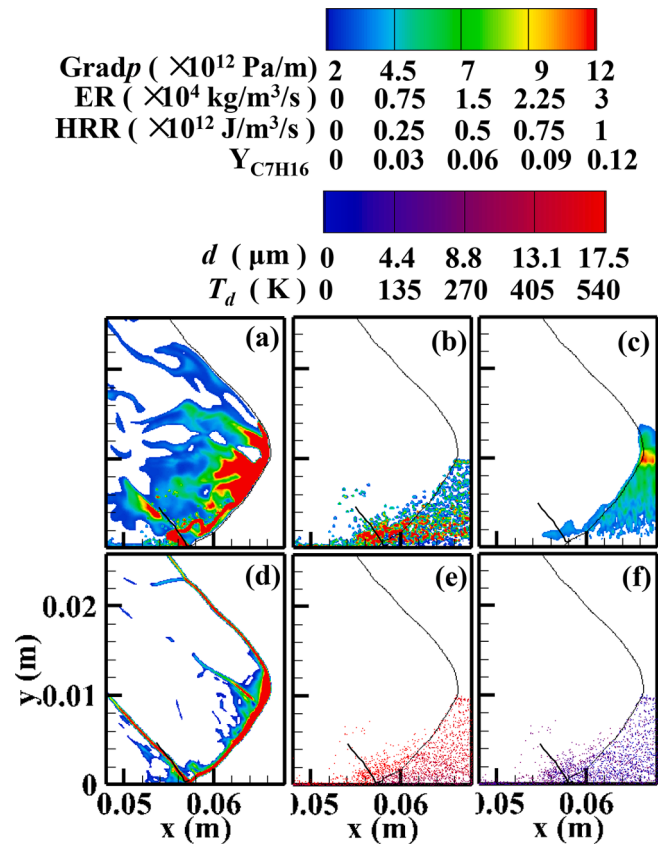


Fig. 7. Contours of (a) heat release rate, (b) evaporation rate, (c) n -heptane vapor mass fraction, (d) pressure gradient magnitude, (e) droplet temperature and (f) diameter. $d_s^0 = 2 \mu\text{m}$ (50%), $d_l^0 = 10 \mu\text{m}$ (50%) and $\phi_t = 1.0$. Solid line: detonation and oblique shock waves.

fraction, pressure gradient magnitude, Lagrangian droplet temperature and diameter near the detonation wave in Fig. 6. More heat release behind the leading shock wave can be found in Fig. 7(a), compared to the counterpart results in Fig. 5(a). This can confirm the effects of the small droplets in fuel vapor supply and hence sustain the detonative combustion. Likewise, local extinctions of the detonation wave can be also observed near the injector in Fig. 7(a). A SRDW along the reflected

shock wave is also present, which is the same as that in Fig. 5(a). The average detonation propagation speed is about 1750 m/s, slightly lower than that in Fig. 2. In Fig. 7, one can also see that the fuel droplets are dispersed almost in the entire fuel refilling area, and this is because 50% of the fuel sprays have larger diameter (10 μm), which have longer heating and evaporation time in the fuel refilling area.

3.2. RDW extinction in fuel sprays

It has been shown from case 2 that the rotating detonative combustion fueled with *n*-heptane sprays are quenched after propagating about five cycles. Their transient will be further discussed in this section, about how the main and secondary rotating detonation wave evolve. Fig. 8 demonstrates the time sequences of pressure and gas temperature during the detonation extinction process. At 1340 μs (same as that in Fig. 4), the RDW still exists. From 1360 μs to 1380 μs , the height of the detonation wave gradually decreases. Moreover, since the pressure behind the detonation wave is higher than the total pressure of the inlet air, the fuel sprays cannot be injected into the combustor, which leads to a gradually reduced fuel filling area. From 1400 μs to 1440 μs , the RDW gradually becomes weak, which can be confirmed by the decreased

temperature and pressure near the detonation wave. Eventually, the detonation wave is extinguished.

Fig. 9 shows the evolutions of the HRR and ER corresponding to the above detonation extinction process. Fig. 9(a)–9(f) correspond to six instants in Fig. 8 (1340 μs –1440 μs). It can be found that the detonation wave undergoes an extinction and re-ignition process. Specifically, at 1340 μs , due to the large droplet diameter, the droplets are unable to evaporate completely in the fuel refilling area and a large amount of evaporating droplets exist after the detonation wave. Existence of these droplets result in a high volumetric evaporation rate in this region. There is a significant discontinuity in the heat release rate on the detonation wave. The detonation wave experiences the first instantaneous extinction.

From Fig. 9(a) to 9(b), although the detonation wave is extinguished, the higher temperature after the wave allows the droplets to continue to evaporate and eventually cause the detonation wave to re-ignite. After that, the heat release behind the leading shock is more distributed, indicating the enhanced detonative combustion, as shown in Fig. 9(b)–(d). Meanwhile, the number of evaporating droplets after the detonation wave gradually increases during this process and eventually leads another severe localized extinction of detonation combustion behind the

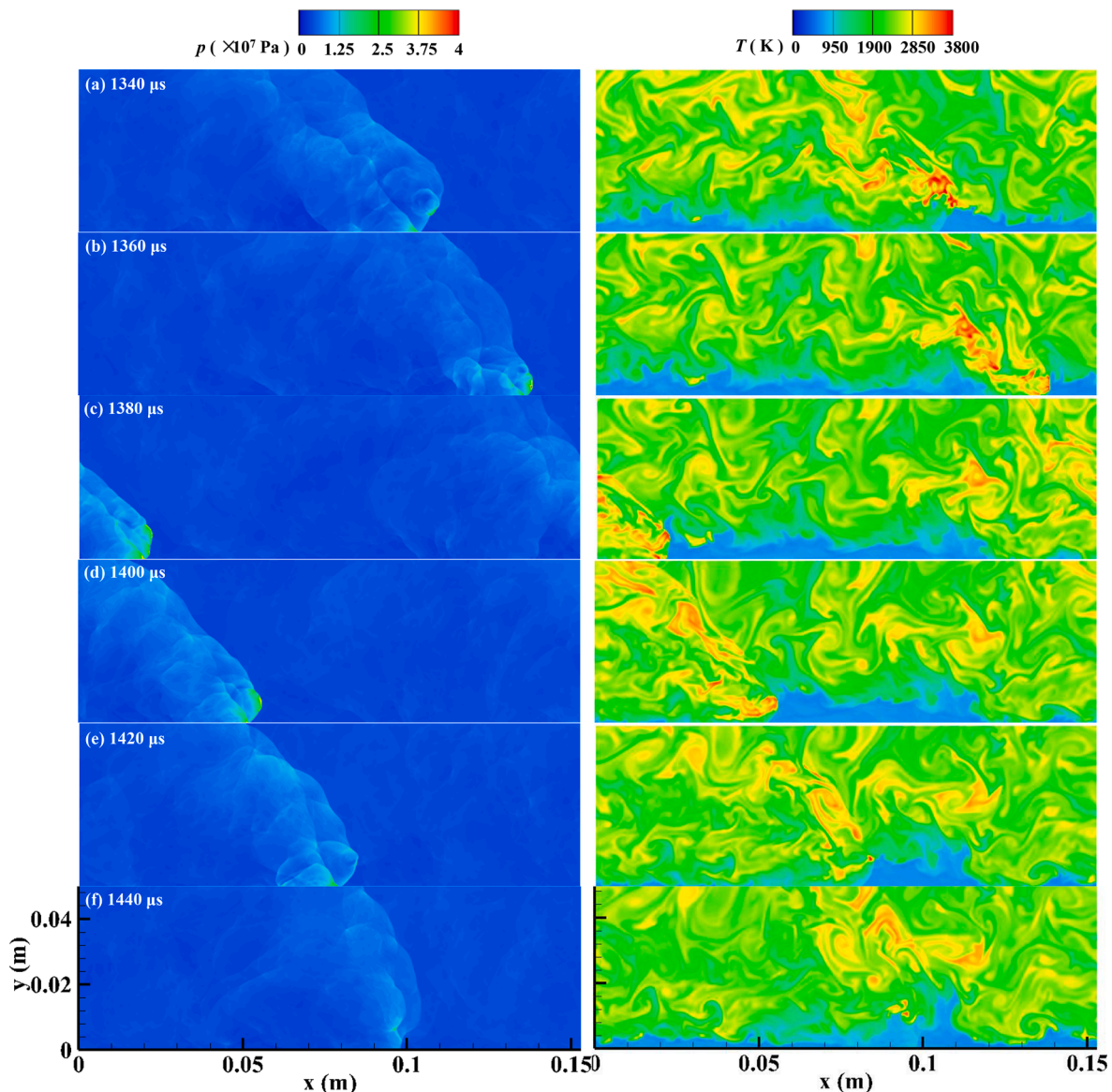


Fig. 8. Extinction process of a detonation wave in *n*-heptane sprays. $d^0 = 10 \mu\text{m}$ and $\phi_t = 1.0$.

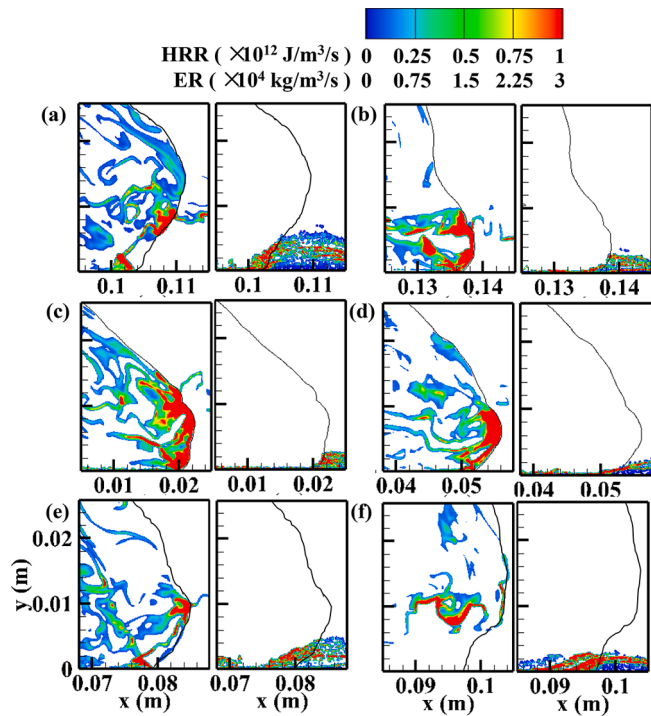


Fig. 9. Time sequence of heat release rate (left column) and evaporation rate (right column) in a detonation extinction process in case 2. Solid line: detonation and oblique shock waves.

leading shock, as shown in Fig. 9(e). Another extinction at 1440 μs can be found in Fig. 9(f). Eventually, the pressure wave is fully decoupled from the combustion wave and the detonation wave is extinguished. Moreover, the height of the secondary detonation wave from the reflected shock wave is low at 1340 μs , about 2 mm (see Fig. 9a). From 1360 to 1380 μs , as the detonation wave is reignited and gradually develops, the height of the secondary detonation wave increases to 5 mm. The secondary detonation wave from the reflected shock also becomes quenched and at 1420 μs , it is no longer observable in Fig. 9(f).

Comparing Fig. 5 and Fig. 7, one can find that when the proportion of

large droplets ϕ_l increases from 50% to 100%, number of the remaining droplets after the detonation wave increases significantly. These residual droplets can continue evaporate behind the detonation wave and the fuel vapour can burn locally with deflagration mode. In these cases, since the total equivalence ratio is the same (1.0), less fuel can be detonated if more fuel is deflagrated. Indeed, we can also see the evaporating droplets behind the detonation wave. However, their percentage is relatively low, and therefore the RDW can still maintain.

3.3. Reactant mixing and detonated fuel fraction

The structure and extinction process of RDW with mono-sized sprays have been discussed in Sections 3.1 and 3.2. In Section 3.3, the effects of larger droplet diameter (d_l^0) in the bi-disperse sprays on reactant mixing, effective equivalence ratio and detonated fuel fraction will be investigated. Fig. 10 shows the contours of *n*-heptane vapor mass fraction and equivalence ratio from the cases of $d_l^0 = 5, 7.5$ and $10 \mu\text{m}$, respectively. $\phi_l = 0.5$ and $d_s^0 = 2 \mu\text{m}$. In this analysis, the effective equivalence ratio ϕ_{eff} is defined as the ratio of required stoichiometric oxygen atoms to the available oxygen atoms [53]. The former is defined as the minimum number of oxygen atoms demanded to convert all carbon and hydrogen atoms to CO_2 and H_2O , respectively [53], i.e.,

$$\phi_{eff} = \frac{n_C + n_H/4}{n_O/2}, \quad (15)$$

where n_C , n_H , and n_O denote the number of available carbon, hydrogen and oxygen atoms, respectively. The reader should be reminded that since it is based on element conservation, ϕ_{eff} is also well defined in the detonation product area. However, the ones in the un-detonated mixtures (such as triangular fuel refilling area) are most relevant for our analysis. Also, only the atoms in the gas phase are considered and no contribution (such as hydrogen or carbon atoms) from the liquid fuels is included.

One can see from Fig. 10 that, as d_l^0 increases from 2 to 10 μm , less vapor is released from the sprayed droplets intermediately after they are injected into the RDE chamber, resulting in less distributions of *n*-C₇H₁₆ vapor near the injectors. As the droplets gradually evaporate downstream of the fuel refilling area, gradual increase of the mass fraction of *n*-C₇H₁₆ vapor can be observed. This is particularly true for $d_l^0 \geq 5 \mu\text{m}$ in

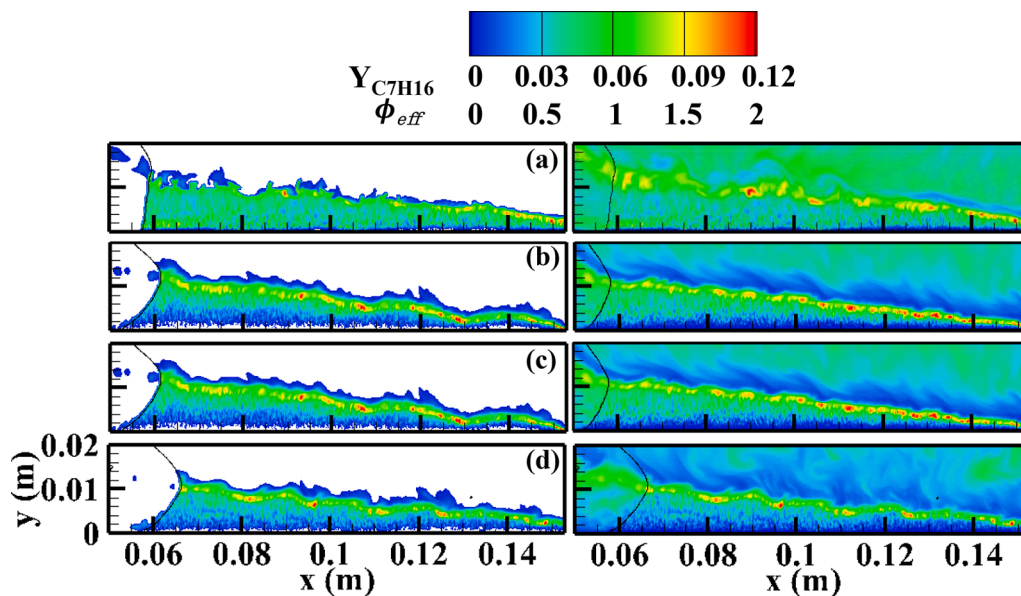


Fig. 10. Contours of (left column) *n*-heptane vapor mass fraction and (right column) effective equivalence ratio: (a) $d_l^0 = 2 \mu\text{m}$, (b) $d_l^0 = 5 \mu\text{m}$, (c) $d_l^0 = 7.5 \mu\text{m}$ and (d) $d_l^0 = 10 \mu\text{m}$. $\phi_l = 0.5$ and $d_s^0 = 2 \mu\text{m}$. Solid line: detonation and oblique shock waves.

Fig. 10(b)–(d). The difference in droplet diameter can lead to a significant difference in the time required for complete evaporation of the droplet. The difference in the distribution of $n\text{-C}_7\text{H}_{16}$ vapor in the fuel refilling area further results in a change of the angle of the detonation wave. As shown in Fig. 10, the detonation wave propagates in a stratified reactant mixtures along the detonation wave height direction, from fuel-lean, to stoichiometric, to spotty fuel-rich compositions along the deflagrative contact surface. Furthermore, in the fuel refilling area, the distance in the y -direction where the equivalence ratio reaches unity increases with the d_l^0 , which ultimately leads to an increase in the angle of the detonation wave with the size of the larger droplet class d_l^0 . n -Heptane vapor is accumulated near the contact surface between the refilled fuel and detonated product, particularly obvious in Fig. 10(b)–(d). The reason for this peculiar phenomenon and its effects on rotating detonations have been explained in Ref. [16].

As shown in Fig. 10, the similar tendencies of the n -heptane vapor inside the fuel refilling area can also be observed from the distributions of the effective equivalence ratio. For $d_l^0 = 2 \mu\text{m}$, overall unity equivalence ratio in the fuel refilling area is found, indicating the fast evaporation and efficient vapor/oxidizer mixing before the detonation wave arrives. However, for the rest cases, the equivalence ratio is almost zero near the top head, and gradually increases towards unity along the y -direction. This is consistent with the results of fuel vapor distributions discussed above. At the fuel-product contact surface, locally rich pockets can be found, with $\phi > 2.0$.

Fig. 11 further quantifies the average equivalence ratio as a function of the diameter d_l^0 of the larger fuel droplet class. Different liquid fuel equivalence ratios (ϕ_{eff}) for larger droplet class are considered, i.e., $\phi_l = 0.2 - 1.0$. Here the averaging is performed based on the fuel refilling area based on ten uncorrelated time instants. Since the droplet evaporation is very limited when they are first injected into the combustor, equivalence ratio around the inlet is almost zero. This makes the average equivalence ratio $\langle\phi_{eff}\rangle$ in the fuel filling area well below 1, with a maximum value of 0.66. As d_l^0 increases, the evaporation rate of the droplets decreases and the area near the inlet with an equivalence ratio close to zero gradually increases. This makes the average equivalence ratio in the fuel filling area gradually decrease.

In the calculation under different proportions of large droplets ϕ_l , when the initial diameter of the larger droplet d_l^0 increases to a certain value, the detonation wave cannot maintain stable propagation. The

maximum droplet diameter before the extinction of the detonation wave is defined as the critical diameter in the following description. The extinction curve is obtained by marking the critical diameters at different ϕ_l . Note that this curve is approximated and in our work we have not performed detailed trail-and-error method to get the accurate results for the extinction conditions. The extinction curve shows that the critical diameter gradually increases as the proportion of large droplets ϕ_l gradually decreases which indicates that decreasing the initial diameter of the droplet is conducive to maintain stable propagation of the detonation wave.

To further interpret the premixedness of the reactants in liquid fueled rotating detonative combustion, the Flame Index (FI) is used here to identify the local combustion regimes, i.e., premixed ($FI = +1$) or non-premixed ($FI = -1$) condition [54]. It is defined as

$$FI = \frac{\nabla Y_F \cdot \nabla Y_O}{|\nabla Y_F| |\nabla Y_O|} \quad (16)$$

where Y_F and Y_O represent the mass fractions of gaseous n -heptane and oxygen, respectively. Fig. 12 shows the contours of flame index in the RDE combustor corresponding to the foregoing four cases. As shown in Fig. 12(a) to 12(d), a value of -1 for FI is found in the fuel refilling area, which implies that the fuel and oxidizer mixing proceeds there. This is in line with the findings from Ref. [17], although the inter-injector spacing is considered therein. However, the deflagration surface and detonation wave are dominated by premixed combustion ($FI = +1$).

The detonated fuel fraction ψ [15,39] is further adopted to measure the percentage of the n -heptane fuel burned by the rotating detonation. It can be estimated from

$$\psi = \frac{\int_V \omega_{t_{C_7H_{16}}} dv}{\int_V \omega_{t_{C_7H_{16}}} dv + \int_V \omega_{f_{C_7H_{16}}} dv} \quad (17)$$

where $\omega_{t_{C_7H_{16}}}$ and $\omega_{f_{C_7H_{16}}}$ are the volumetric consumption rates of detonated and deflagrated $n\text{-C}_7\text{H}_{16}$, respectively. V represents the computational domain. Note that the n -heptane fuel is deemed denoted (deflagrated) when the corresponding heat release rate is greater than or approximately equal to (less than) $10^{13} \text{ J/m}^3/\text{s}$ [55]. This value is determined from a stand-alone C-J n -heptane detonation calculation with The Shock & Detonation Toolbox [56]. When we slightly adjust the foregoing criterion around this numerical value, the obtained detonated fuel fraction is almost not affected. This shows the limited sensitivity of

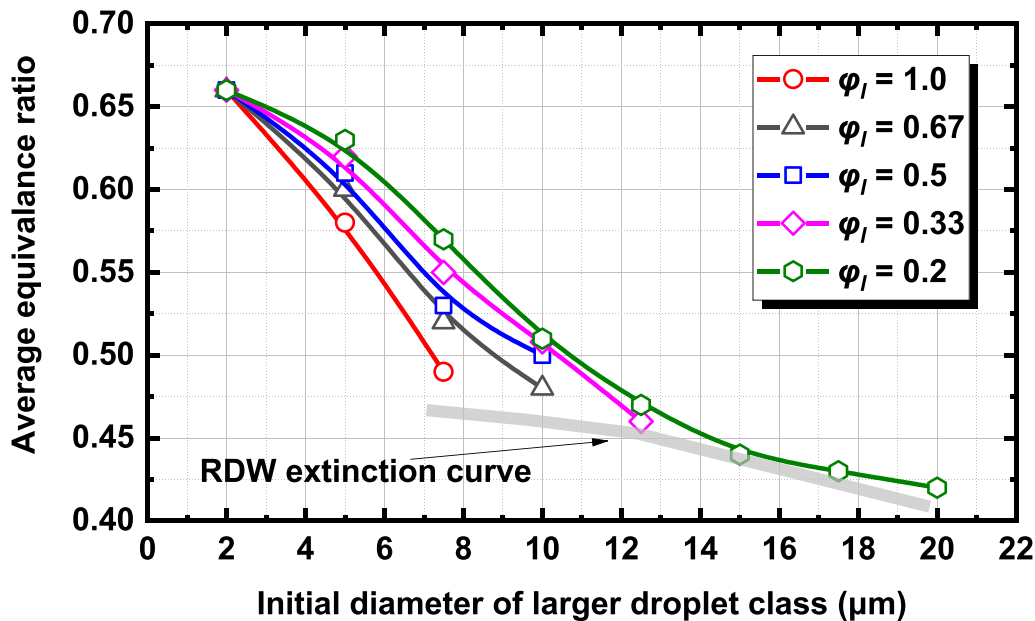


Fig. 11. Average equivalence ratio in the fuel refilling area as a function of the diameter of larger droplet class. $d_s^0 = 2 \mu\text{m}$ and $\phi_t = 1.0$.

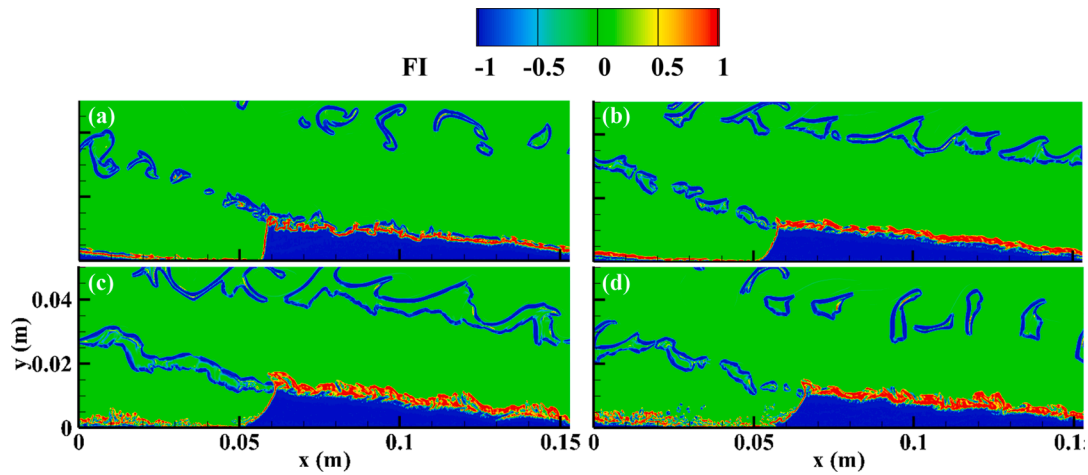


Fig. 12. Contours of flame index in the combustor: (a) $d_l^0 = 2 \mu\text{m}$, (b) $5 \mu\text{m}$, (c) $7.5 \mu\text{m}$ and (d) $10 \mu\text{m}$. $\phi_l = 0.5$ and $d_s^0 = 2 \mu\text{m}$.

ψ to the HRR criterion.

Fig. 13 shows the change of detonated fuel fraction ψ as a function of the diameter d_l^0 of the larger fuel droplet class. For comparison, the result of gaseous RDC with $\phi = 1.0$ (i.e., full vaporization before injection) is also shown. The detonated fuel fraction ψ in the simulated liquid fuel RDE are 6%–18% lower than that (0.9) of the corresponding gaseous RDE. Overall, regardless of the larger droplet equivalence ratio ϕ_l , the detonated fuel fraction ψ monotonically decreases with increased d_l^0 . This is because as the diameter d_l^0 increases, the droplets do not evaporate quickly after being injected into the combustor. There are large amount of fuel droplets crossing the detonation wave and continuing evaporating there. The released vapor mixes with the local oxidizer and is deflagrated (HRR is below $10^{13} \text{ J/m}^3/\text{s}$). As d_l^0 increases, the droplets behind the detonation wave increases, which would lead to reduced detonated fuel fraction ψ . This trend is observed all the larger droplet equivalence ratio ϕ_l .

Moreover, as ϕ_l increases, from instance, from 0.2 to 1.0, the diameter of the largest droplets with which a stable detonation wave can be sustained gradually decreases. Besides, under the same d_l^0 ($< 7.5 \mu\text{m}$), ψ increases as ϕ_l decreases. Decreased ϕ_l indicates increased fraction of small droplets ($d_s^0 = 2 \mu\text{m}$) that can be fully evaporated and which can contribute towards the detonative combustion, which will increase ψ .

3.4. Detonation wave propagation speed

Fig. 14 shows the change of the detonation propagation speed with the diameter of the larger droplets d_l^0 in bi-dispersed sprays. The total liquid fuel equivalence ratio ϕ_t is 1 for all considered cases. For comparison, the result of gaseous RDC with $\phi_t = 1.0$ (i.e., full vaporization before injection) is also added. It is found that the detonation propagation speeds from liquid fueled RDC are 4%–10% lower than that of the corresponding gaseous RDC. There may be different reasons for the speed deficits, such as nonuniform mixing of oxidizer and fuel in the fuel filling area, and heat or momentum exchange due to the droplets near the detonation front [17]. As d_l^0 increases, the detonation propagation speed gradually decreases in all the cases with various ϕ_l . This is because the larger the size of the fuel droplet, the lower the average equivalence ratio in the fuel filling area, and the propagation velocity of the detonation wave decreases as the equivalence ratio decreases. Under the same equivalence ratio ϕ_l , the small droplets can release more vapor than the large size droplets, and therefore the detonation propagation speed is higher.

The RDW velocity deficit at different d_l^0 is given in Fig. 15. The velocity deficit is calculated as $\delta v = (v_g - v_d)/v_g$, where v_g is the velocity of gaseous detonation at the same total pressure and temperature, whilst v_d is that of two-phase detonations at different d_l^0 . As shown in Fig. 15, the

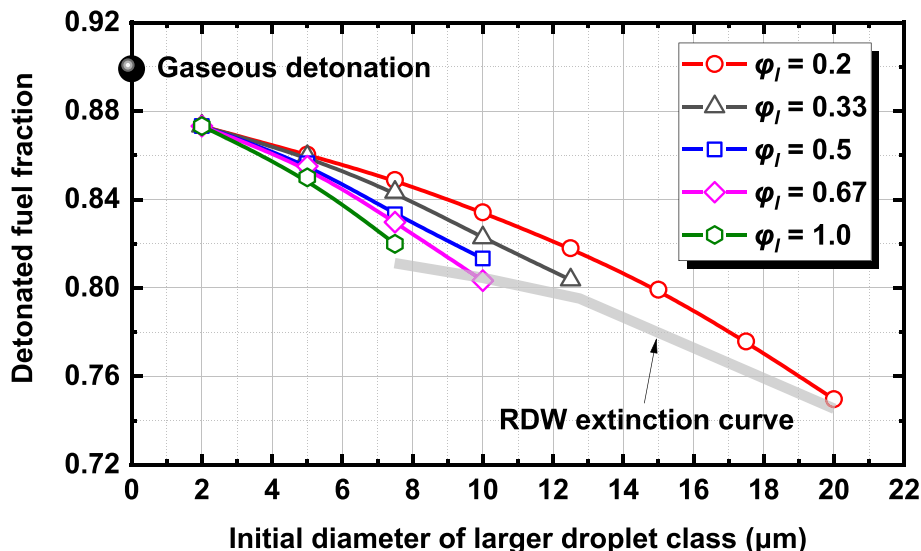


Fig. 13. Detonated fuel fraction as a function of the diameter of larger droplets. $d_s^0 = 2 \mu\text{m}$ and $\phi_t = 1.0$.

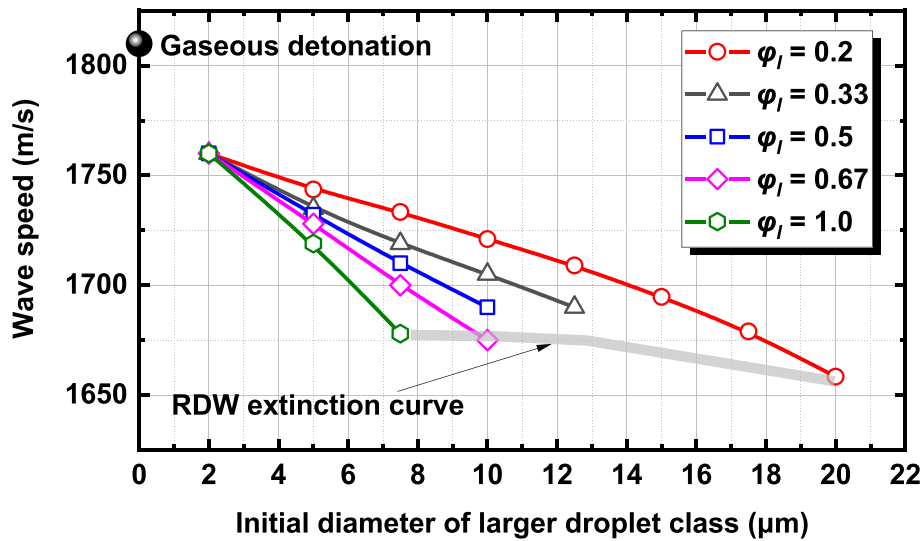


Fig. 14. Detonation wave speed as a function of the droplet diameter. $d_s^0 = 2 \mu\text{m}$ and $\phi_t = 1.0$.

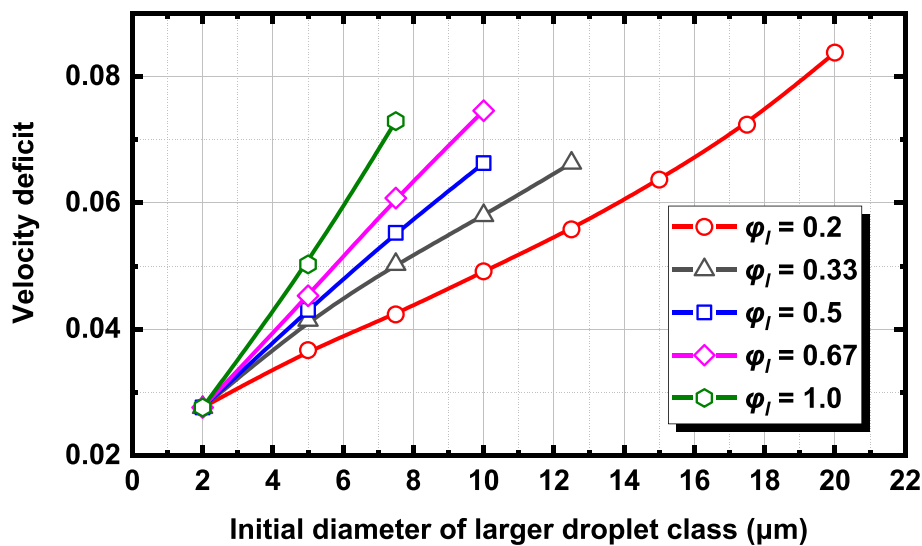


Fig. 15. Velocity deficit as a function of the droplet diameter. $d_s^0 = 2 \mu\text{m}$ and $\phi_t = 1.0$.

droplets need to evaporate into gaseous *n*-heptane mixing with air in the fuel refilling area, which makes the distribution of the equivalence ratio in the fuel refilling area non-uniform, as shown in Fig. 10. This non-uniform distribution makes the speed of the detonation wave lower than that of the gaseous detonation under the same conditions. As d_l^0 increases, *n*-heptane vapor yield in the fuel refilling area decreases, and accordingly the equivalence ratio in the fuel-refilling area decreases, which makes the detonation wave speed decrease and the velocity deficit increases. Moreover, as the equivalence ratio of larger droplet classes ϕ_l increases, the number of droplets increases, the equivalence ratio in the fuel-refilling area decreases, and hence the velocity deficit gradually increases.

3.5. Propulsion performance

The droplet diameter and spatial distribution in the RDE chamber not only affect the detonation wave propagation, but also the propulsion performance resulting from the detonation combustion. To this end, the specific impulse I_{sp} is calculated

$$I_{sp} = \int_{A_o} [\rho u^2 + (p - p_b)] dA_o / g \dot{m}_F \quad (18)$$

in which A_o is the area of the outlet, u is the gas velocity at the outlet, \dot{m}_F is the mass flow rate of the fuel, g is gravity acceleration, p is the local pressure at the outlet, and p_b is the backpressure. Fig. 16 shows the effect of diameter d_l^0 and equivalence ratio ϕ_l of the larger droplet class on the specific impulse I_{sp} . Specifically, for a given equivalence ratio (such as $\phi_l = 0.5$), as d_l^0 increases, the specific impulse gradually decreases. This is because as d_l^0 increases, when the droplets are sprayed into the combustor, they cannot quickly evaporate into a gaseous state. This further affects the overall ratio of detonation combustion and hence reduces specific impulse. For a fixed diameter of larger droplet class (such as $d_l^0 = 5 \mu\text{m}$), as ϕ_l increases, the number of droplets with a diameter of $2 \mu\text{m}$ decreases, which means that the number of droplets that can completely evaporate into fuel vapor in the fuel refilling area decreases. The decrease in the number of droplets decreases the average equivalence ratio in the fuel refilling area, which leads to a decrease in specific impulse.

The thrust force from the kinetic energy and pressure gain in rotating

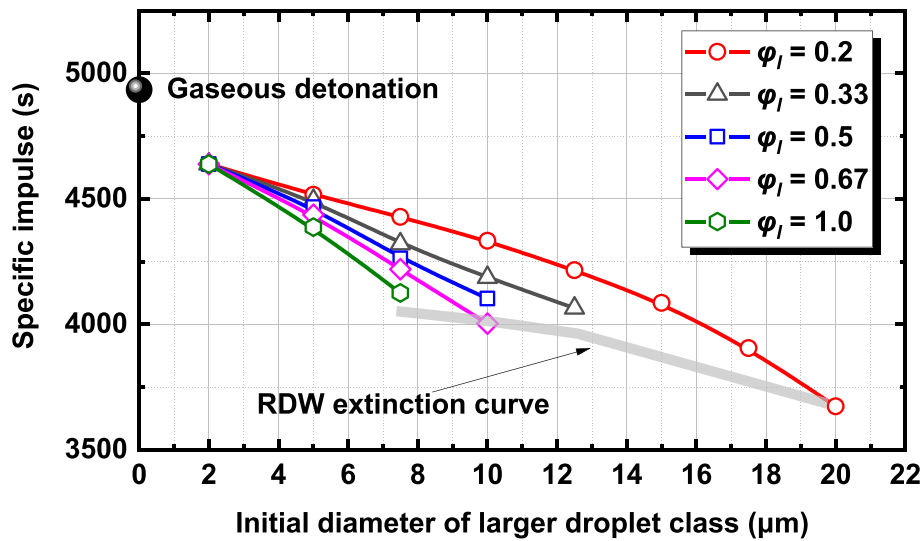


Fig. 16. Specific impulse as a function of droplet diameter. $d_s^0 = 2 \mu\text{m}$ and $\phi_l = 1.0$.

detonations are also shown in Fig. 17. The thrust from kinetic energy is defined as $F_u = \int_{A_o} \rho u^2 dA_o$, whilst the thrust from pressure gain is $F_p = \int_{A_o} (p - p_b) dA_o$. The thrust from kinetic energy includes the thrust generated by combustion products as well as by the propellant itself. The thrust generated by combustion products is the thrust from the pressure gain and it is the more important one in the two types of thrust described above, which can be clearly observed in the Fig. 17. The thrust force from pressure gain F_p decreases significantly with the droplet diameter d_l^0 . As d_l^0 increases, the droplet evaporation rate decreases, and the unburned droplets after the detonation wave gradually increases, resulting in deflagration combustion of *n*-heptane vapor near the slip line. This reduces the detonated fuel fraction ψ (see Eq. (17)) and eventually leads to a decrease in thrust. For a fixed diameter of larger droplet class (such as $d_l^0 = 5 \mu\text{m}$), as ϕ_l increases, the average equivalence ratio $\langle \phi_{eff} \rangle$ in the fuel refilling area decreases, which leads to a decrease in the detonated fuel fraction and ultimately to a decrease in thrust from pressure gain. Since the propellant flow rate is not changed in the calculations of this study, this means that the kinetic energy of the propellant produces almost no change in thrust for different operating conditions, so the

trend of F_u is the same as F_p .

From the above results, we can see that droplet diameter and the mass ratio of the larger droplet class are important factors for droplet evaporation and heating, thereby stabilizing the two-phase rotating detonations. Specifically, if both d_l^0 and ϕ_l are high (such as case 2 in Section 3.1), the detonation wave would extinguish due to relatively slow evaporation rate. If both d_l^0 and ϕ_l are small (such as case 1), the detonation wave can propagate stably due to sufficient fuel vapour supply from the liquid fuels and the propagation and propulsion characteristics of the detonation wave are higher than other conditions (the d_l^0 is small but ϕ_l is high or d_l^0 is high but ϕ_l is small, as will be shown later). If the d_l^0 is small but ϕ_l is high or d_l^0 is high but ϕ_l is small, although the remaining droplets can be observed after the detonation wave, the propagation of the detonation wave is still stable from our simulated case. This, to some degree, corroborates the role of the fine droplet class in stabilizing the detonation wave. However, the propagation and propulsion characteristics of the detonation wave are lower than those of case 1 in which both d_l^0 and ϕ_l are small.

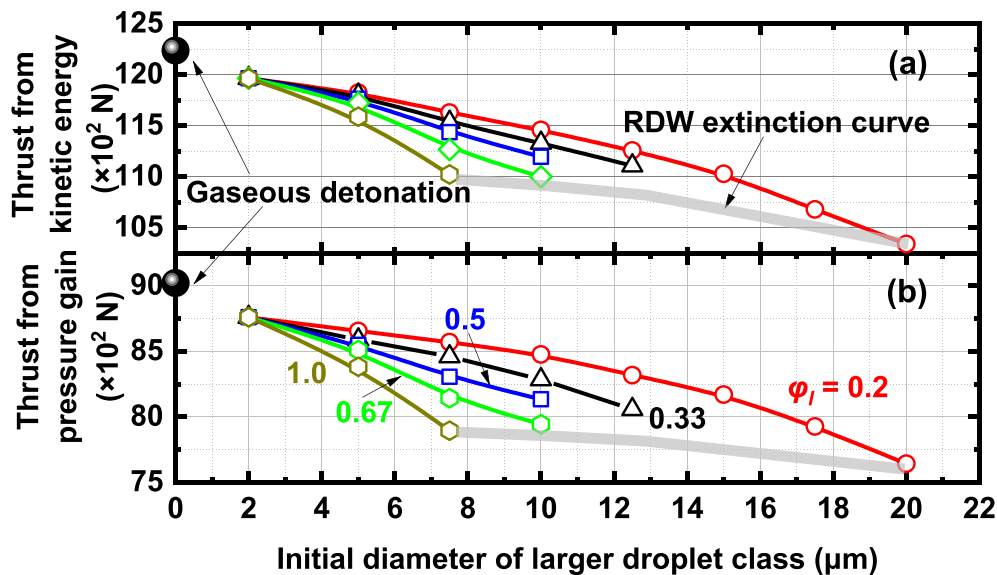


Fig. 17. Thrust force from (a) kinetic energy and (b) pressure gain. $d_s^0 = 2 \mu\text{m}$ and $\phi_l = 1.0$.

4. Conclusions

Two-dimensional rotating detonations fueled by liquid *n*-heptane sprays are simulated with Eulerian – Lagrangian method. Bi-disperse fuel droplets without any fuel pre-vaporization are considered in our work and parametric studies are performed to clarify the influences of liquid fuel droplet diameter and equivalence ratio on rotating detonation wave propagation, reactant mixing and propulsion performance.

In mono-sized sprays, when the droplet diameter is small (2 μm), the *n*-heptane droplets can completely evaporate in the fuel refilling area. While droplet diameter increases, a reflected shock can be observed after the detonation wave and the larger droplets can not completely evaporate in the fuel refilling area and exist behind the detonation wave. When the droplet diameter is $>10 \mu\text{m}$, the higher pressure after the detonation wave leads to the reactants can not be sprayed into the combustor eventually leading to the extinction of the detonation wave. In bi-disperse sprays with 50% droplets of $d_s^0 = 2 \mu\text{m}$ and 50% large droplets of $d_l^0 = 10 \mu\text{m}$, the presence of droplets with small diameter maintains the stable propagation of the detonation wave, while reflected shock is also observed.

The incomplete evaporation of droplets in the fuel filling area near the inlet of the RDC leads to an average equivalence ratio in the fuel refilling area (ϕ_{eff}) lower than ϕ_t . ϕ_{eff} decreases with increasing d_l^0 and the decreasing ϕ_{eff} leads to a decrease in the detonated fuel fraction with increased d_l^0 . The detonation propagation speeds from liquid fueled RDC are lower than that of the corresponding gaseous RDC. The increase in d_l^0 and ϕ_l raise the velocity deficit. Finally, d_l^0 and ϕ_l also affect the thrust and specific impulse of the RDC. The propulsive performance decreases with increased d_l^0 and ϕ_l .

CRedit authorship contribution statement

Shan Jin: Conceptualization, Methodology, Writing – original draft, Visualization, Investigation. **Huangwei Zhang:** Writing – review & editing, Supervision, Project administration, Funding acquisition. **Ningbo Zhao:** Supervision. **Hongtao Zheng:** Supervision.

Declaration of Competing Interest

The authors declare that they have no known competing financial interests or personal relationships that could have appeared to influence the work reported in this paper.

Acknowledgements

The simulations used the ASPIRE 1 Cluster from National Supercomputing Centre, Singapore (NSCC) (<https://www.nsc.sg/>). SJ is supported by China Scholarship Council (No. 202006680045). HZ is supported by MOE Tier 1 grant (R-265-000-653-114). Discussion with Dr Majie Zhao from Beijing Institute of Technology is gratefully acknowledged.

References

- [1] Wolański P. Detonative propulsion. *Proc Combust Inst* 2013;34(1):125–58.
- [2] Anand V, Gutmark E. Rotating detonation combustors and their similarities to rocket instabilities. *Prog Energy Combust Sci* 2019;73:182–234.
- [3] Bykovskii FA, Zhdan SA, Vedernikov EF. Continuous spin detonations. *J Propuls Power* 2006;22(6):1204–16. <https://doi.org/10.2514/1.17656>.
- [4] Rankin BA, Richardson DR, Caswell AW, Naples AG, Hoke JL, Schauer FR. Chemiluminescence imaging of an optically accessible non-premixed rotating detonation engine. *Combust Flame* 2017;176:12–22. <https://doi.org/10.1016/j.combustflame.2016.09.020>.
- [5] Bykovskii FA, Zhdan SA, Vedernikov EF. Continuous spin detonation of fuel-air mixtures. *Combust Explos Shock Waves* 2006;42(4):463–71. <https://doi.org/10.1007/s10573-006-0076-9>.
- [6] Shen P-W, Adamson Jr TC. Theoretical analysis of a rotating two-phase detonation in liquid rocket motors. *NASA* 1972.
- [7] Bykovskii FA, Zhdan SA, Vedernikov EF. Continuous spin detonation of a heterogeneous kerosene–air mixture with addition of hydrogen. *Combust Explos Shock Waves* 2016;52(3):371–3.
- [8] Bykovskii FA, Zhdan SA, Vedernikov EF. Continuous detonation of the liquid kerosene–air mixture with addition of hydrogen or syngas. *Combust Explos Shock Waves* 2019;55(5):589–98.
- [9] Kindracki J. Experimental studies of kerosene injection into a model of a detonation chamber. *J Power Technol* 2012;92:80–9.
- [10] Kindracki J. Experimental research on rotating detonation in liquid fuel–gaseous air mixtures. *Aerosp Sci Technol* 2015;43:445–53.
- [11] Wolański P, Balicki W, Perkowski W, Bilal A. Experimental research of liquid-fueled continuously rotating detonation chamber. *Shock Waves* 2021;31(7):807–12.
- [12] Sun Bo, Ma Hu. Two-dimensional numerical study of two-phase rotating detonation wave with different injections. *AIP Adv* 2019;9(11):115307.
- [13] Hayashi AK, Tsuboi N, Dzieminska E. Numerical study on JP-10/air detonation and rotating detonation engine. *AIAA J* 2020;58(12):5078–94.
- [14] Ren Z, Zheng L. Numerical study on rotating detonation stability in two-phase kerosene-air mixture. *Combust Flame* 2021;231:111484.
- [15] Meng Q, Zhao M, Zheng H, Zhang H. Eulerian-Lagrangian modelling of rotating detonative combustion in partially pre-vaporized *n*-heptane sprays with hydrogen addition. *Fuel* 2021;290:119808.
- [16] Meng Q, Zhao N, Zhang H. On the distributions of fuel droplets and in situ vapor in rotating detonation combustion with prevaporized *n*-heptane sprays. *Phys Fluids* 2021;33(4):043307.
- [17] Zhao M, Zhang H. Rotating detonative combustion in partially pre-vaporized dilute *n*-heptane sprays: droplet size and equivalence ratio effects. *Fuel* 2021;304:121481.
- [18] Smirnov NN, Nikitin VF, Dushin VR, Filippov YG, Nerchenko VA, Khadem J. Combustion onset in non-uniform dispersed mixtures. *Acta Astronaut* 2015;115:94–101.
- [19] Smirnov NN, Betelin VB, Kushnirenko AG, Nikitin VF, Dushin VR, Nerchenko VA. Ignition of fuel sprays by shock wave mathematical modeling and numerical simulation. *Acta Astronaut* 2013;87:14–29.
- [20] Betelin VB, Smirnov NN, Nikitin VF, Dushin VR, Kushnirenko AG, Nerchenko VA. Evaporation and ignition of droplets in combustion chambers modeling and simulation. *Acta Astronaut* 2012;70:23–35.
- [21] Smirnov NN, Nikitin VF, Khadem J, Alyari-Shourekhdli Sh. Onset of detonation in polydispersed fuel–air mixtures. *Proc Combust Inst* 2007;31(2):2195–204.
- [22] Reid RC, Prausnitz JM, Poling BE. The properties of gases and liquids. McGraw Hill Book; 1987.
- [23] McBride BJ. Coefficients for calculating thermodynamic and transport properties of individual species. *Natl Aeron Space Administr* 1993;4513.
- [24] Crowe CT, Sharma MP, Stock DE. The particle-source-in cell (PSI-CELL) model for gas-droplet flows 1977;99:325–32.
- [25] Sazhin SS. Advanced models of fuel droplet heating and evaporation. *Prog Energy Combust Sci* 2006;32(2):162–214.
- [26] Tyurenkova VV. Non-equilibrium diffusion combustion of a fuel droplet. *Acta Astronaut* 2012;75:78–84.
- [27] Tyurenkova V. Two regimes of a single *n*-heptane droplet combustion. *Acta Astronaut* 2019;163:25–32.
- [28] Abramzon B, Sirignano WA. Droplet vaporization model for spray combustion calculations. *Int J Heat Mass Transf* 1989;32(9):1605–18.
- [29] Fuller EN, Schettler PD, Giddings JC. A new method for prediction of binary gas-phase diffusion coefficients. *Ind Eng Chem* 1966;58(5):18–27.
- [30] Liu AB, Mather D, Reitz RD. Modeling the effects of drop drag and breakup on fuel sprays. *SAE Trans* 1993:83–95.
- [31] Naumann Z, Schiller L. A drag coefficient correlation. *Z Ver Deutsch Ing* 1935;77:318–23.
- [32] Ranz WE, W. R. Marshall J. Evaporation from Drops, Part I. *Chem Eng Prog* 1952;48:141–6.
- [33] Xu Y, Zhao M, Zhang H. Extinction of incident hydrogen/air detonation in fine water sprays. *Phys Fluids* 2021;33(11):116109.
- [34] Sato T, Chacon F, White L, Raman V, Gamba M. Mixing and detonation structure in a rotating detonation engine with an axial air inlet. *Proc Combust Inst* 2021;38(3):3769–76.
- [35] Betelin VB, Nikitin VF, Mikhachenko EV. 3D numerical modeling of a cylindrical RDE with an inner body extending out of the nozzle. *Acta Astronaut* 2020;176:628–46.
- [36] Smirnov NN, Nikitin VF, Stamov LI, Mikhachenko EV, Tyurenkova VV. Three-dimensional modeling of rotating detonation in a ramjet engine. *Acta Astronaut* 2019;163:168–76.
- [37] Smirnov NN, Nikitin VF, Stamov LI, Mikhachenko EV, Tyurenkova VV. Rotating detonation in a ramjet engine three-dimensional modeling. *Aerosp Sci Technol* 2018;81:213–24.
- [38] Hishida M, Fujiwara T, Wolanski P. Fundamentals of rotating detonations. *Shock Waves* 2009;19(1):1–10.
- [39] Zhao M, Cleary MJ, Zhang H. Combustion mode and wave multiplicity in rotating detonative combustion with separate reactant injection. *Combust Flame* 2021;225:291–304.
- [40] Zhang H, RYrhoCentralFOAM, <https://blog.nus.edu.sg/huangwei-nus-ryrhoCentralfoam-solver/>, National University of Singapore.
- [41] Greenshields CJ, Weller HG, Gasparini L, Reese JM. Implementation of semi-discrete, non-staggered central schemes in a colocated, polyhedral, finite volume framework, for high-speed viscous flows. *Int J Numer Methods Fluids* 2010;63:1–21.

- [42] Huang Z, Zhao M, Xu Y, Li G, Zhang H. Eulerian-Lagrangian modelling of detonative combustion in two-phase gas-droplet mixtures with OpenFOAM: Validations and verifications. *Fuel* 2021;286:119402.
- [43] Zhang H, Zhao M, Huang Z. Large eddy simulation of turbulent supersonic hydrogen flames with OpenFOAM. *Fuel* 2020;282:118812.
- [44] Zhao M, Ren Z, Zhang H. Pulsating detonative combustion in n-heptane/air mixtures under off-stoichiometric conditions. *Combust Flame* 2021;226:285–301.
- [45] Liu S, Hewson JC, Chen JH, Pitsch H. Effects of strain rate on high-pressure nonpremixed n-heptane autoignition in counterflow. *Combust Flame* 2004;137(3):320–39.
- [46] Reitz RD. Modeling atomization processes in high-pressure vaporizing sprays. *At Spray Technol* 1987;3:309–37.
- [47] Crowe CT, Sommerfeld M, Tsuji Y. *Multiphase flows with particles and droplets*. New York: CRC Press; 1998.
- [48] Watanabe H, Matsuo A, Matsuoka K, Kawasaki A, Kasahara J. Numerical investigation on propagation behavior of gaseous detonation in water spray. *Proc Combust Inst* 2019;37(3):3617–26.
- [49] Sontheimer M, Kronenburg A, Stein OT. Grid dependence of evaporation rates in Euler-Lagrange simulations of dilute sprays. *Combust Flame* 2021;232:111515.
- [50] Luo K, Desjardins O, Pitsch H. DNS of droplet evaporation and combustion in a swirling combustor. *Cent Turbul Res Annu Res Briefs* 2008:253–65.
- [51] Smirnov NN, Betelin VB, Nikitin VF, Stamov LI, Altoukhov DI. Accumulation of errors in numerical simulations of chemically reacting gas dynamics. *Acta Astronaut* 2015;117:338–55.
- [52] Smirnov NN, Betelin VB, Shagaliev RM, Nikitin VF, Belyakov IM, Deryuguin YN, et al. Hydrogen fuel rocket engines simulation using LOGOS code. *Int J Hydrogen Energy* 2014;39(20):10748–56.
- [53] Zhou R, Hochgreb S. The behaviour of laminar stratified methane/air flames in counterflow. *Combust Flame* 2013;160(6):1070–82.
- [54] Yamashita H, Shimada M, Takeno T. A numerical study on flame stability at the transition point of jet diffusion flames. *Symp Combust* 1996;26(1):27–34.
- [55] Zhao M, Li J-M, Teo CJ, Khoo BC, Zhang H. Effects of variable total pressures on instability and extinction of rotating detonation combustion. *Flow, Turbul Combust* 2020;104(1):261–90.
- [56] Shepherd J. *Shock and Detonation Toolbox*. <https://shepherd.caltech.edu/EDL/PublicResources/sdt/>.